Structure/Processing Relationships of Highly Ordered Lead Salt Nanocrystal Superlattices

Tobias Hanrath,[†,*] Joshua J. Choi,[‡] and Detlef-M. Smilgies[§]

[†]School of Chemical and Biomolecular Engineering, [‡]School of Applied and Engineering Physics, and [§]Cornell High Energy Synchrotron Source (CHESS), Cornell University, Ithaca, New York 14853

ABSTRACT We investigated the influence of processing conditions, nanocrystal/substrate interactions and solvent evaporation rate on the ordering of strongly interacting nanocrystals by synergistically combining electron microscopy and synchrotron-based small-angle X-ray scattering analysis. Spin-cast PbSe nanocrystal films exhibited submicrometer-sized supracrystals with face-centered cubic symmetry and $(001)_s$ planes aligned parallel to the substrate. The ordering of drop-cast lead salt nanocrystal films was sensitive to the nature of the substrate and solvent evaporation dynamics. Nanocrystal films drop-cast on rough indium tin oxide substrates were polycrystalline with small grain size and low degree of orientation with respect to the substrate, whereas films drop-cast on flat Si substrates formed highly ordered face-centered cubic supracrystals with close-packed $(111)_s$ planes parallel to the substrate. The spatial coherence of nanocrystal films drop-cast in the presence of saturated solvent vapor was significantly improved compared to films drop-cast in a dry environment. Solvent vapor annealing was demonstrated as a postdeposition technique to modify the ordering of nanocrystals in the thin film. Octane vapor significantly improved the long-range order and degree of orientation of initially disordered or polycrystalline nanocrystal assemblies. Exposure to 1,2-ethanedithiol vapor caused partial displacement of surface bound oleic acid ligands and drastically degraded the degree of order in the nanocrystal assembly.

KEYWORDS: nanocrystals · self-assembly · surface-induced orientation · vapor annealing · *in situ* and real-time characterization · grazing-incidence small-angle X-ray scattering

Colloidal nanocrystal (NC) research is rapidly moving beyond the synthesis of materials with well-defined size, shape, and composition toward the controlled assembly of nanoscale building blocks into ordered and functional structures. The prospect of combined control over individual and ensemble nanocrystal (NC) properties provides a rich opportunity space for the engineering of metamaterials with coherent electrical and optical properties relevant to a number of nanotechnology applications including electrical,[1,2] optical,[3] and sensor-type devices.[4] As in analogous molecular systems, collective interactions among NCs in these artificial solids are strongly influenced by NC energy levels, coupling between adjacent sites, and the symmetry and spacing of the lattice.[5]

These aspects are particularly pronounced in lead salt (PbX; X = S, Se, Te) NCs, rendering these materials an ideal experimental testbed for three reasons. First of all, PbSe NCs are among the most strongly quantum confined systems. Thanks to the large Bohr diameter of the exciton (46 nm),[6,7] adjusting the NC diameter between 1 and 10 nm provides experimental control to prepare materials with a tunable energy gap ranging from 1.7 to 0.4 eV, respectively.[8−12] Second, the strong electron and hole wave function overlap facilitate strong quantum mechanical coupling of proximate NC cores. Consequently, reducing the interparticle separation, for instance *via* chemical treatments to exchange or displace the long insulating ligands, has been shown to dramatically influence the electronic and optical properties of lead salt NC films.[13−15]

The third feature that promotes lead salt NCs as an experimentally advantageous system for the study of functional NC assemblies is the strong dipole−dipole coupling between individual NCs. The dipoles are believed to arise from an uneven distribution of Pb and Se terminated {111} facets of individual NCs[16] or charged surface states.[17] Strong dipole interactions are absent in "weakly coupled" metal NCs and in the case of lead salt NCs have been considered as the driving force in the formation of highly anisotropic nanostructures, *via* oriented attachment,[18,19] and the assembly of NC films with nonclose packed, simple-hexagonal, symmetry.[20] Klokkenburg *et al.* recently estimated the strength of the dipolar pair attraction to be in the range of 8−10 k_BT on the basis of a statistical analysis of one-dimensional aggregates formed in room-temperature NC suspensions.[21] Taken together, these observations provide a

*Address correspondence to th358@cornell.edu.

Received for review June 9, 2009 and accepted August 30, 2009.

Published online September 3, 2009. 10.1021/nn901008r CCC: $40.75

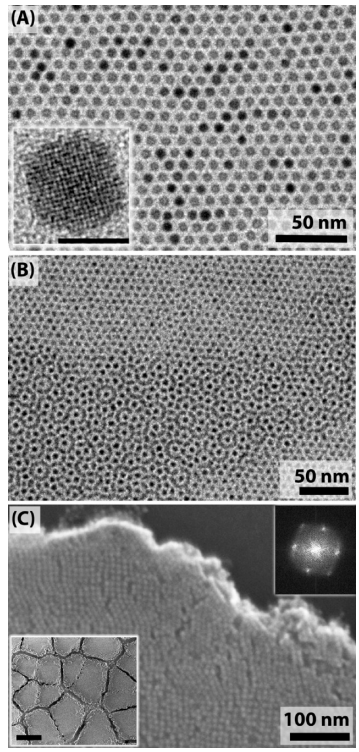

Figure 1. Nanocrystal assemblies. TEM images of (A) monolayer. Inset: high resolution image of a single nanocrystal, scale = 5 nm. (B) Partial bilayer deposited onto a TEM grid. (C) SEM image of a thick multilayer deposited onto a Si wafer. Upper inset: FFT pattern showing the regionally nonhexagonal ordering of the superlattice. Lower inset: low resolution SEM image showing characteristic crack pattern of the thin film, scale bar = 10 μm.

strong incentive to study and ultimately control the NC assembly processes.

Using PbSe and PbS NCs as a model system, we investigated the influence of processing conditions, evaporation and diffusion dynamics, and the nature of the substrate on the spatial coherence of the deposited NC films. We combined transmission and scanning electron microscopy (TEM/SEM) and synchrotron based grazing-incidence small-angle X-ray scattering (GISAXS) to gain insights into the fundamental parameters governing NC supracrystal assembly and the internal thin film stresses leading to the formation of microscopic cracks. Lastly, we demonstrate solvent vapor annealing as a new approach to improve the long-range spatial coherence of NC assemblies.

RESULTS AND DISCUSSION

NC Characterization. The electron micrographs in Figure 1 illustrate the evolution of complex morphologies encountered in NC assemblies going from monolayer to partial bilayers and multilayered thin films. The formation of well-ordered monolayers, as seen in Figure 1A, is predicated on NC samples with a narrow size distribution. Fortunately, the hot-injection method pioneered by Murray and co-workers[22] offers robust and facile synthesis of colloidal NCs with size distributions ≤10% without the need for postsynthesis size-selective precipitation.

The ordering of the second NC layer is strongly influenced by the structure of the NC monolayer underneath. If interactions among the particles are weak, the particles in the second layer can be modeled as hard spheres and assemble in the entropically favored interstitial spaces (*i.e.*, the troughs) of the first layer—a configuration commonly found in spherical colloids.[23] The partial bilayer PbSe NC assembly in Figure 1B however shows a complex, but systematic deviation from the ideal close-packed structure. In the case of metal NCs, similar bilayer structures have been attributed to the faceted nature of nonspherical NCs and strong van der Waals attractions between the NC cores.[24,25] In colloidal lead salt NCs, similar faceting may also play a role; however, the strong dipolar interactions between adjacent NCs introduce another perturbation that must be considered to understand the energetic driving forces behind NC ordering.

The transition from bilayers to multilayered NC films with thicknesses on the order of tens to hundreds of nanometers introduces an even greater level of complexity. Two important aspects of NC films are captured in the SEM image in Figure 1c. First, the NC film exhibits a micrometer sized fractal pattern reminiscent of cracks found in dried mud or paint (see lower inset Figure 1C). The formation of cracks during the drying of thin films is a well-known phenomenon reoccurring at multiple length scales.[26] Fundamentally, such cracks arise from the concurrent volume reduction and adhesion to the underlying substrate which creates lateral stresses within the evaporating thin film that are ultimately relaxed through the formation of cracks.

At the nano- to micrometer length scale, similar crack formation in NC films due to film drying effects and chemical treatments has emerged as a vexing challenge in the processing of a variety of NC-based prototype test structures.[13,27−31] For example, metal evaporation on discontinuous, cracked NC films can lead to detrimental short circuits. The continued path toward functional NC-based films would tremendously benefit from improved processing techniques that permit the controlled formation of crack-free NC assemblies or crack-healing at multimicrometer length scales.

The second notable aspect of these NC films shown in Figure 1C is the ordering of constituent particles on the nanometer scale. The SEM image shows a micrometer-sized grain of a NC supracrystal. At higher magnification, several defects, mostly in the form of vacancies, can be observed. Near the edge of the supracrystal, the ordering of the NCs is more complex than the simple hexagonal symmetry expected for close-packed $(111)_s$ planes of a face-centered cubic (FCC) supracrystal. Instead, the Fourier transform in the upper right inset of Figure 1C can be indexed to a distorted $[011]_s$ projection of a FCC supracrystal. Similar

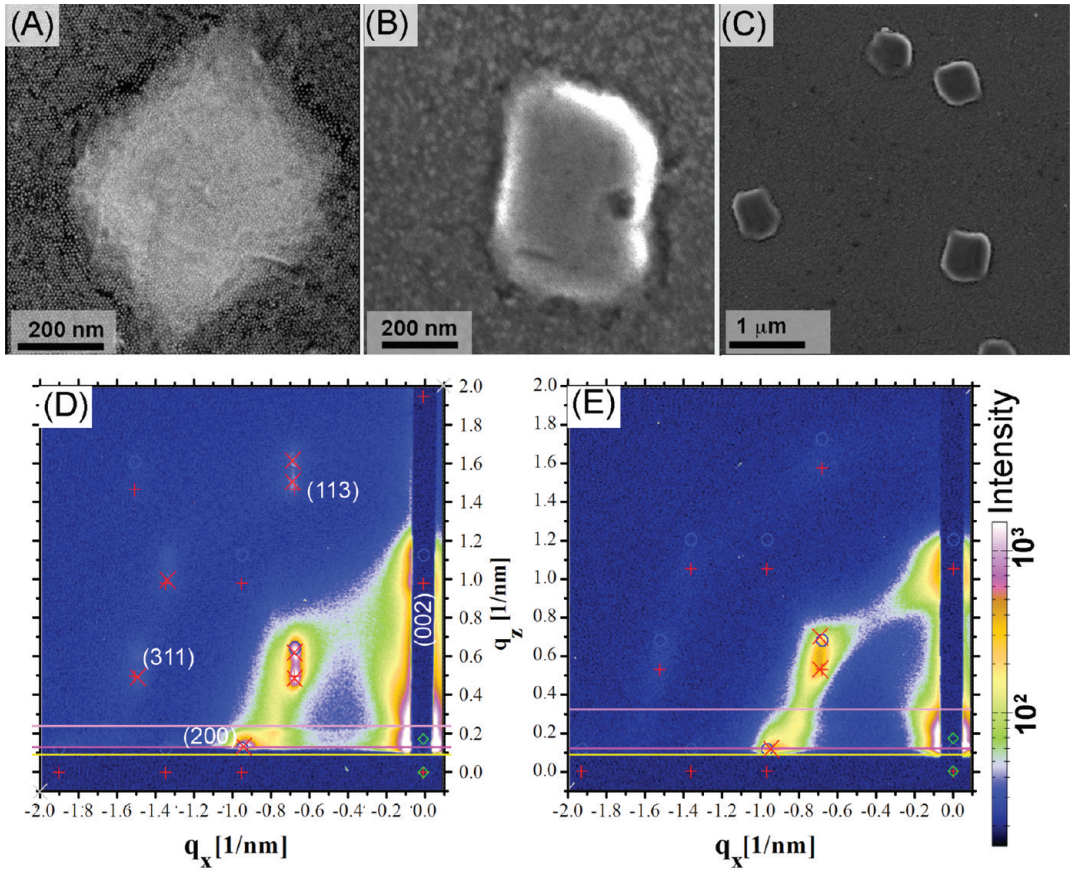

Figure 2. Spin-cast PbSe NC films. High-resolution SEM images of PbSe NC film spun onto (A) Si and (B) ITO. (C) Low-magnification SEM image of PbSe NC film spun cast onto Si. Corresponding GISAXS patterns of NC films on (C) Si and (D) ITO.

variations in supracrystal ordering have previously been reported in Au and Ag NC films by Sigman *et al.*[32] However, electron microscopy alone is incapable of providing an unambiguous differentiation between a distorted $[011]_s$ projection of a FCC supracrystal, or a different (non-FCC) lattice symmetry altogether.[33] *Vis-à-vis* the sensitive relationship between the interparticle quantum mechanical coupling and the symmetry and spacing of the supracrystal, there is a critical need to fully capture the three-dimensional complexity of these assemblies over multiple length scales.

The examples in Figure 1 illustrate that neither transmission nor scanning electron microscopy can provide the level of detailed structural feedback required to understand and ultimately control the formation of functional NC supracrystals. To fill this gap, grazing-incidence small-angle X-ray scattering (GISAXS) has emerged as a powerful tool for the structural characterization of lateral and normal ordering at the surface and inside nanostructured thin films.[34−54]

In the structural analysis of NC films, small-angle X-ray scattering parallel to the substrate surface provides information about the lateral ordering and the scattering perpendicular to the substrate yields information about the ordering of NCs along the substrate normal. Well-defined scattering peaks indicate NC assemblies with specific orientations with respect to the substrate, while ringlike scattering features indicate random or polycrystalline orientation of the NC.[35,38,39] Below, we illustrate the application of GISAXS, combined with electron microscopy, to elucidate the role of processing conditions and substrate/NC interactions in the assembly of strongly interacting lead salt NCs. Our study focused on substrates relevant to the fabrication of NC-based optoelectronic prototype test structures.

Substrate and Deposition Effects. The choice of colloidal NC deposition method depends on multiple factors. Although spin-casting is the method of choice for most organic thin films, the formation of homogeneous NC films with smooth surfaces and high spatial coherence has favored alternative methods including Langmuir films,[55] drop casting,[22,56,57] dip-coating,[58,59] or slow evaporation on tilted substrates.[20,48] These techniques provide control over a broader range of solvent evaporation rates and are more compatible with additional solution-based processing methods that often accompany NC thin-film processing.[59,60]

We compared the structural properties and spatial coherence of NC films prepared by spin-casting and controlled evaporation drop-casting. Figure 2A,B shows high-resolution SEM images and corresponding GISAXS patterns of NC films formed by spin-casting a 50 mg/mL

suspension onto Si wafers and indium−tin-oxide (ITO) substrates, respectively. We found submicrometer-sized square and rectangular shapes as a common feature of NC film spun onto both Si and ITO substrates. Similar structures, identified as $(001)_s$ oriented supracrystals were previously reported by Murray *et al.* in slowly evaporated CdSe NC films.[61] Tilted high-resolution SEM images revealed that these structures were relatively flat with a *ravioli*-like shape (see Supporting Information Figure S1).

Figure 2B shows the SEM image of similar rectangular structures found in PbSe NC film spun-cast onto ITO. Fast Fourier transform (FFT) analysis of high-resolution SEM image in Figure 2A reveals a square symmetry within the *ravioli*-shaped supracrystal, whereas the surrounding partial bilayer NC film shows a hexagonal symmetry (see Supporting Information Figure S2). The FFT analysis of SEM images thus provides important first insights into the diversity of NC spatial coherence observed in spun-cast films and shows that the lateral orientations of the square and hexagonal NC assemblies were unrelated. Figure 2B shows the SEM image of similar rectangular structures found in PbSe NC film spun-cast onto ITO. We were unable to resolve the lattice structure of NC films on ITO *via* FFT SEM image analysis, presumably due to the roughness of the conducting oxide substrate. Nevertheless, the similarity of submicrometer rectangular shapes and GISAXS patterns (*vide infra*) suggests that NC films spun cast onto ITO had a similar symmetry and spatial coherence as the NC films deposited onto silicon wafers covered with native oxide.

To precisely determine the supracrystal symmetry and spacing of both the ravioli-shaped structure and the hexagonal NC layer background, we acquired GISAXS patterns to complement the SEM images. Figure 2C and 2D show GISAXS patterns of the NC films spun-cast onto Si and ITO, respectively. Both patterns show two strong scattering peaks near $q_x = -0.7$ nm^{-1}. The corresponding azimuthally and radially integrated intensity profiles are shown in the Supporting Information (Figure S3). The bright band of intensity marking the onset of the scattering pattern is related to the Yoneda effect,[62] that is, enhanced scattering at the critical angle. To delineate between direct scattering and reflected beam scattering signatures of the NC film,[63] we acquired scattering patterns at a series of incident angles (see supporting info Figure S4). Furthermore, we can differentiate the scattering pattern of the *ravioli*-shaped supracrystals from the signatures of NC background layer with hexagonal symmetry by comparing the data in Figure 2 to GISAXS patterns of a partial NC monolayer (see Supporting Information Figure S5). These controls allow us to uniquely identify the specific lattice structure of the *ravioli*-shaped supracrystal based on four distinguishing scattering features: (1) the $(311)_s$ and $(131)_s$ peaks near $q_x \approx -1.5$; $q_z \approx 0.4$ nm^{-1}, (2) the $(113)_s$ peak near $q_x \approx -0.7$; $q_z \approx 1.4$ nm^{-1}, (3) the $(200)_s$ and $(020)_s$ peaks near $q_x \approx -0.95$; $q_z \approx 0.1$ nm^{-1} (partially obscured by the Yoneda band), and last (4) the $(002)_s$ peak near $q_x = 0$; $q_z \approx 0.95$ nm^{-1} (partially blocked by the beam stop).

On the basis of a least-squares fit of these scattering features, we index the GISAXS pattern in Figure 2C to a $(001)_s$ oriented FCC supracrystal with 2% shrinkage normal to the plane of the substrate. The shrinkage transforms the FCC lattice to a lower-symmetry tetragonal lattice. Such uniaxial shrinkage has been reported for a number of different systems cast from solution, such as block copolymers,[45] nanocomposites,[46] and NC superlattices,[47,48] and seems to be a common feature of soft materials that are cast from solution.

The observation of ravioli shaped $(001)_s$ oriented supracrystals in PbSe NC film spun onto substrates with substantially different surface roughness (Si root-mean-square (rms) roughness ≈ 0.16 nm and ITO rms ≈1.8 nm; see Supporting Information Figure S6) strongly suggests that NC/substrate interactions play a negligible role in the formation of these supracrystals. Alternatively, these supracrystals could have nucleated at either the rapidly receding vapor−liquid interface or within the liquid volume colloidal NC suspension. To delineate the effects of colloidal NC concentration and rapid solvent evaporation accompanying spin-casting, we spun PbSe NC films from serially diluted NC suspensions. We found that ravioli-shaped supracrystals only formed from spin-casting concentrated (50 mg/mL) suspensions, whereas dilute suspensions (0.5−5.0 mg/mL) resulted in hexagonally ordered submonolayers (see Supporting Information Figure S7). Moreover, we recently measured GISAXS spectra of colloidal NC suspension *in situ* and found no scattering signatures indicative of $(001)_s$ supracrystals near the nucleation threshold.[64] Taken together, these observations suggest that a concentrated NC suspension and rapid evaporation are coupled necessary conditions for the formation of $(001)_s$ oriented supracrystals.

To explain the formation of ravioli-shaped supracrystals we considered energetic and kinetic aspects of superlattice nucleation. At equilibrium, the surface energies in FCC crystals rank as $\gamma_{(111)} < \gamma_{(100)} < \gamma_{(110)}$; however, the surface energy of (001) facets is only marginally above those of (111) facets. We therefore attribute the formation of $(001)_s$, ravioli supracrystal nuclei as an indication of dominant kinetic effects related to the fast processing dynamics inherent to spin-casting. This interpretation is consistent with a previous report by Bawendi and co-workers,[65] who showed that hexagonal NC ordering in spun-cast films originates at the rapidly receding liquid/vapor interface and not at the interface between the liquid and the solid substrate. A similar mechanism (*i.e.*, nucleation at the rapidly receding liquid/vapor interface) is most likely to

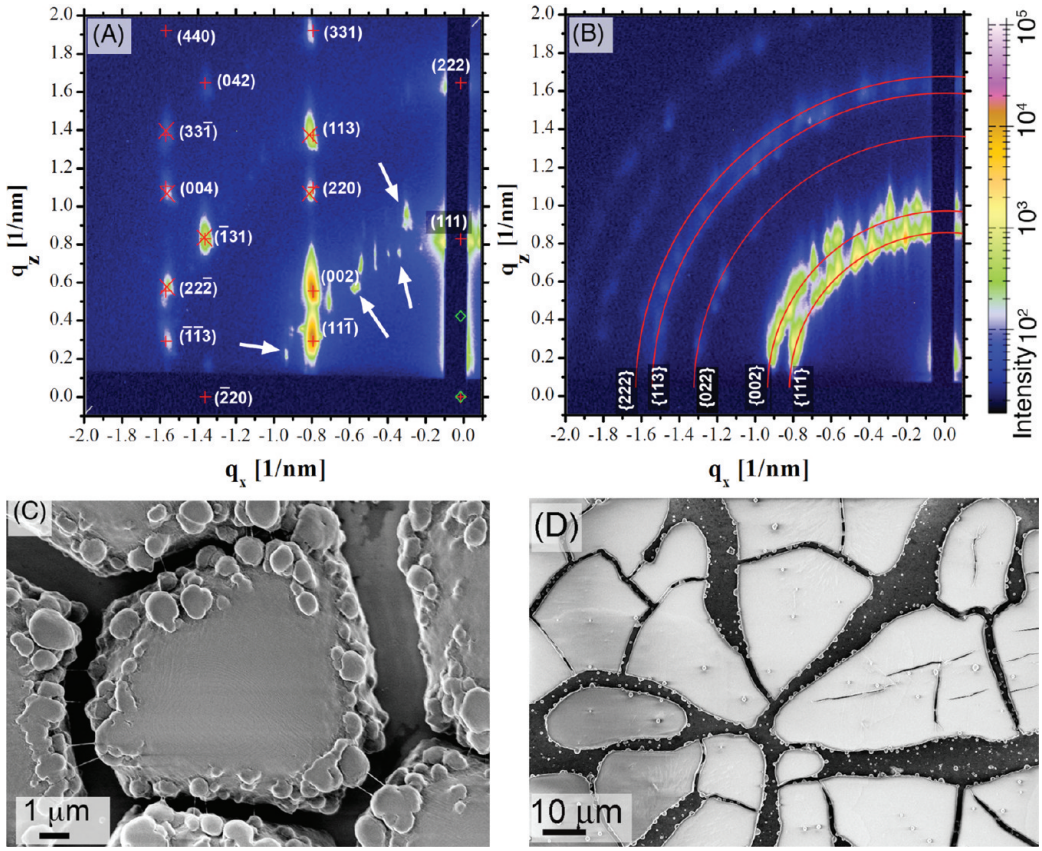

Figure 3. Drop-cast PbSe NC films. GISAXS patterns of (A) highly oriented NC film on Si and (B) polycrystalline NC film on ITO substrate. Spot indices (A) for a (111) oriented FCC lattice or FCC powder rings (B) are indicated. (C) SEM image of large NC supracrystal grain on Si and (D) SEM image of cracked NC film on ITO.

have led to the ravioli-shaped PbSe NC supracrystals observed in this study.

While the structure of spin-cast NC films shows only modest correlation to the roughness of the substrate, we found that NC/substrate interactions plays a much more prominent role in the assembly of drop-cast films. We drop-cast lead salt NCs onto ITO and Si substrates from a 50 mg/mL suspension in a controlled vapor environment and allowed the suspension to interact with the substrate for a predetermined time before the top of the funnel was unplugged (see Supporting Information). This procedure allows us to control the solvent evaporation rate (*i.e.*, the film drying dynamics) and allowed the solvent to gradually diffuse and evaporate.

Figure 3A shows the GISAXS pattern of a PbSe NC film prepared by drop-casting the NC suspension onto a silicon wafer and gradually letting the solvent evaporate after 60 min of incubation time. The presence of multiple, well-defined scattering peaks allowed us to precisely determine the superlattice symmetry including lattice dimensions and distortions formed during the drying stages of the film deposition. The precision of this approach has previously been successfully demonstrated in lattice deformations in polymer films, NC assemblies, and nanocomposites.[44−48] We applied multiple-peak least-squares fitting and indexed the scattering pattern in Figure 3A to a $(111)_s$ oriented FCC supracrystal with a lattice constant a of 13.2 nm. We note that the supracrystal lattice spacing measured in these drop-cast, $(111)_s$ oriented NC films is consistent with the superlattice spacing determined for the spin-cast, $(001)_s$ supracrystals discussed above.

Unlike the vertical shrinkage in binary NC superlattices recently reported by Korgel and co-workers,[48] the optimum fit to the PbSe NC superlattice scattering in Figure 3 was obtained for an undeformed (*i.e.*, 0% shrinkage) FCC supracrystal. The absence of vertical lattice shrinkage suggests that PbSe NC films prepared by slow-evaporation drop-casting dried with an isotropic reduction of the film volume. This observation is corroborated by the extensive cracking observed in these films and suggests that the cohesion between NCs is stronger than their adhesion to the substrate. We will address film drying and crack formation in more detail below.

Aside from the strong FCC scattering signatures, the GISAXS pattern of the PbSe NC film drop-cast onto Si (Figure 3A) also exhibits weaker secondary peaks (white arrows) which we attribute to minor polycrystalline domains. This interpretation is also supported by the SEM image in Figure 3C showing a large (~10 μm) supracrystal grain with several satellite grains near the edge. Additional SEM images showing steps and ter-

races of the single supracrystal grains are provided in the Supporting Information (Figure S8).

NC films drop-cast in a saturated vapor environment onto ITO substrates show a ringlike scattering signature indicative of a polycrystalline film without specific grain orientation (Figure 3B). The azimuthally integrated scattering intensity profile shows well-defined peaks corresponding to the spacing of low index $\{111\}_s$ and $\{002\}_s$ planes observed in the highly ordered FCC supracrystal formed on Si (see Supporting Information Figure S9). The radial width of the reflections shows that crystallites of the NC film on ITO were of similar size as in the oriented films on Si. Radially integrated intensity profiles, on the other hand, show that PbSe NC supracrystals formed by drop casting onto Si wafers exhibit a markedly higher degree of orientation relative to the substrate surface than similarly prepared NC films on ITO (see Supporting Information Figure S9B). Moreover, low-resolution SEM images show a microscopic crack pattern with rounded grains, distinct from the polygonal cracks observed in NC films deposited onto Si (see Supporting Information Figure S8). The grain size in both oriented and unoriented NC supracrystals is approximately 130 nm based on Scherrer equation analysis of the scattering peak width.

Notably, the GISAXS images of NC films on ITO (Figure 3B) show several sharp scattering peaks superimposed on a ringlike background. To determine whether these are due to randomly oriented supracrystals or surface induced structures, we probed the NC film at 1 mm intervals across a 8 mm long section of the sample. The superposition of these spectra and the radially integrated intensity plots show that the distinct peaks are not random with respect to the azimuthal angle (ϕ) or lateral film position, but instead exhibit several consistent features (see Supporting Information Figure S10). This observation points toward surface induced ordering resulting from the interactions between the NCs and the ITO substrate. The observed power pattern clearly has FCC structure; however, the origin of the preferred grain orientation associated with the azimuthal peaks remains to be identified.

Beyond the topographical aspects of the deposition surface, chemical NC/substrate interactions have to be considered in the formation of NC assemblies. Yan *et al.*[66] recently showed that the extent of NC ordering can be significantly influenced by Coulombic interactions between charged surfaces and NCs. To probe whether similar interactions were involved in our system, we investigated the ordering of PbSe NC films on chemically distinct, but topographically similar, substrates. We focused on ITO and poly(3,4-ethylenedioxythiophene):poly(styrenesulfonate) (PEDOT:PSS) films because of their widespread use as substrates in NC-based optoelectronic test structures. In contrast to the neutral surface of the conducting oxide substrate, PEDOT:PSS films, with an excess of the latter component, are slightly negatively charged.[67] Based on the work by Yan *et al.*,[66] negatively (positively) charged PbSe NCs should therefore exhibit increased (decreased) degree of ordering on PEDOT-coated substrates.

NC films drop-cast onto on PEDOT-coated and bare ITO substrates exhibited qualitatively similar ringlike GISAXS features composed of superimposed polycrystalline diffraction spots (see Supporting Information Figure S11). Two features distinguished NC films on PEDOT from those deposited onto bare ITO: (1) NC films drop-cast on PEDOT exhibited slightly more pronounced higher order scattering, and (2) radially integrated intensity profiles show a distinct scattering distribution as a function of azimuthal angle (ϕ) (see Supporting Information Figure S11D). A common feature of NC films deposited on PEDOT and ITO was a slight vertical distortion (*i.e.*, along q_z) of the superimposed polycrystalline scattering peaks. Since the NC film thickness ($\sim$2 μm) is much larger than the domain size calculated from the Scherrer equation ($\sim$0.10 μm), we interpret this distortion as an indication of better spatial coherence in the plane of the substrate, than in the normal direction.[68] Overall, we attribute the qualitative similarity of NC films on PEDOT:PSS and ITO to either the relatively high roughness of both surfaces (PEDOT rms = 1.63 nm; ITO rms $\approx$ 1.8 nm) or to the negligible Coulombic NC/surface interactions. Similar to the NC films on ITO, we have not yet identified the origin of specific grain orientations; however, the lattice formed is again clearly FCC.

Drying Time Effects. We exploited ambient vapor concentration as an experimental parameter to adjust the solvent evaporation rate and thereby gain more insight into the mechanism and dynamics of NC supracrystal formation. In the case of fast evaporation in a dry ambient, the rate at which the liquid−vapor interface approaches the substrate surface, known as the interface velocity, exceeds the diffusion rate of NCs within the suspension. Conversely, if the evaporation rate (*i.e.*, interface velocity) is slowed down in the presence of a saturated vapor environment, the NC assembly dynamics are governed by diffusion. To compare the relative impact of the liquid/vapor interface velocity and NC diffusion in the liquid, we adopted a model by Jaeger and co-workers.[69]

In the case of a 100 μL drop drying on a 1 cm^2 substrate in a dry environment, the liquid film thickness shrinks approximately 1 mm/4 min = 250 μm/min. This distance is approximately twice the average vertical diffusion distance during the first minute, which can be estimated by $(2Dt)^{1/2} \approx 125$ μm. The diffusion constant, D, can be approximated by the Stokes−Einstein relation $D = k_BT/3\pi\eta d$, where $\eta = 0.35$ cP is the approximate viscosity of hexane/octane (9:1, v:v) mixture and $d = 10$ nm, the hydrodynamic diameter of the NC. Alternatively, if the liquid evaporation rate is delayed in the case of a saturated vapor environment, the assembly

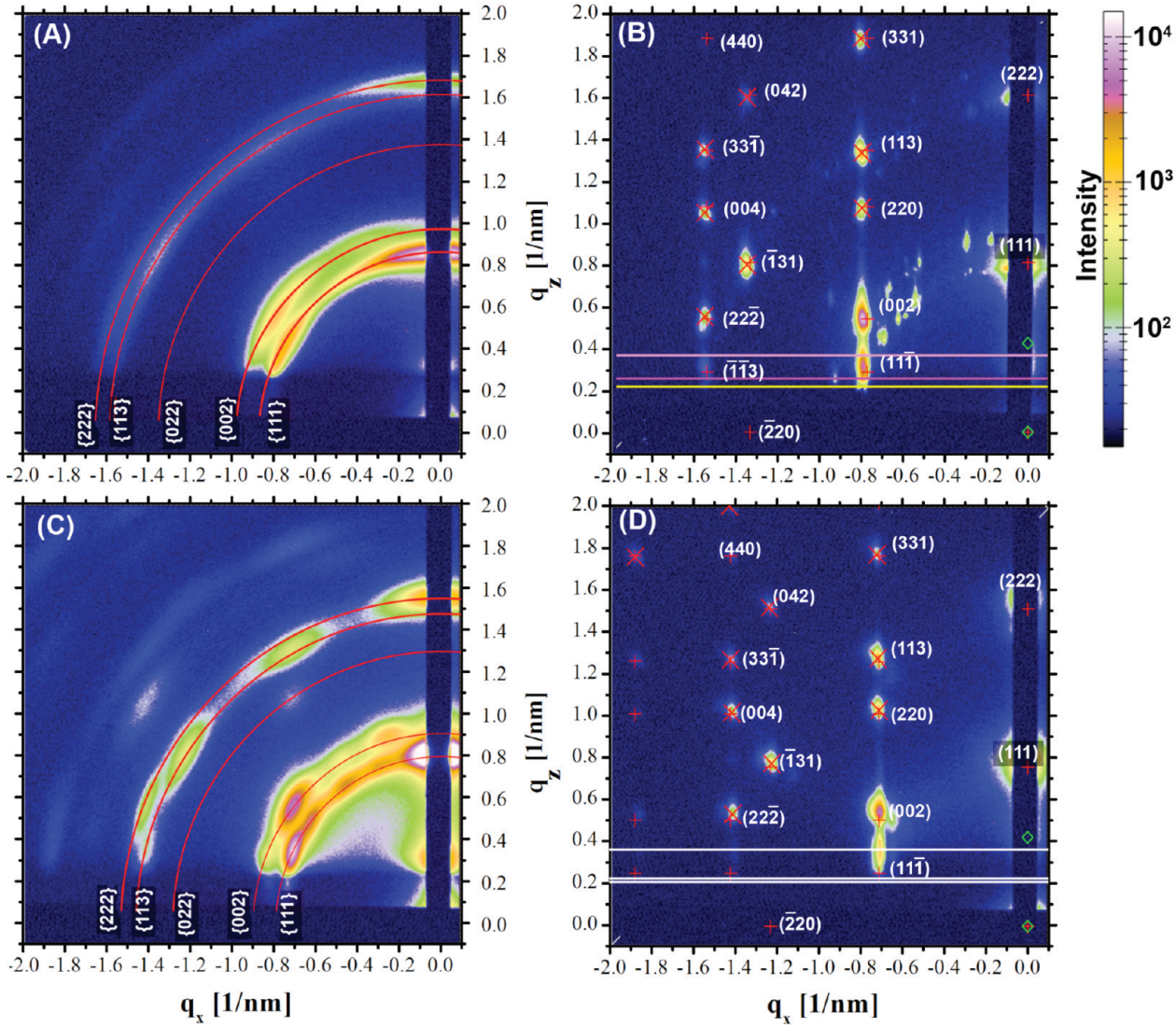

Figure 4. The effect of evaporation time. GISAXS pattern of a drop-cast PbSe NC film dried within (A) 4 min and (B) 60 min. Corresponding drop-cast PbS NC films dried within (C) 4 min and (D) 60 min.

dynamics will be governed by diffusion of NCs within the colloidal suspension.

To illustrate the effect of modified solvent evaporation rates, we compared the ordering in NC films prepared with fast and slow solvent evaporation. Figure 4A and 4B show GISAXS patterns of PbSe NC films prepared from a 5 mg/mL solution with a fast (4 min) and slow (60 min) drying times. The GISAXS pattern of the fast-dried film shows ringlike scattering patterns indicative of a "polycrystalline" structuring of the NC assembly with substrate-induced texture. NC films prepared with a slow drying time (60 min), by drop-casting in a saturated vapor environment, showed dramatically improved long-range ordering and grain orientation. Based on a least-squares fit of the 10 most intense reflections we indexed the PbSe NC film to a FCC supracrystal (a = 13.3 nm; 0% shrinkage) with $(111)_s$ planes parallel to the substrate surface. Based on this lattice identification, we assign the ringlike scattering features of the fast-dried NC film in Figure 4A to the $\{111\}_s$, $\{002\}_s$, and $\{222\}_s$ planes.

In a complementary set of experiments, we investigated the impact of drying-time on the ordering of similarly sized (d = 6.4 nm) PbS NC films. We found that PbS supracrystals exhibited a higher degree of orientation than corresponding films prepared from PbSe NCs. This observation holds for both films prepared with long and short drying times. Compared to the powderlike scattering pattern of the fast-dried PbSe NC film (Figure 4A), PbS NC films prepared under identical conditions show more distinct scattering features superimposed on a powderlike background (Figure 4C). The slowly dried PbS NC film exhibited a remarkable degree of orientational order as indicated by the sharp higher-order scattering peaks and the absence of polycrystalline signatures (Figure 4D). The GISAXS pattern can again be indexed to a FCC supracrystal with a lattice constant of 14.4 nm with a minor (1.4%) vertical lat-

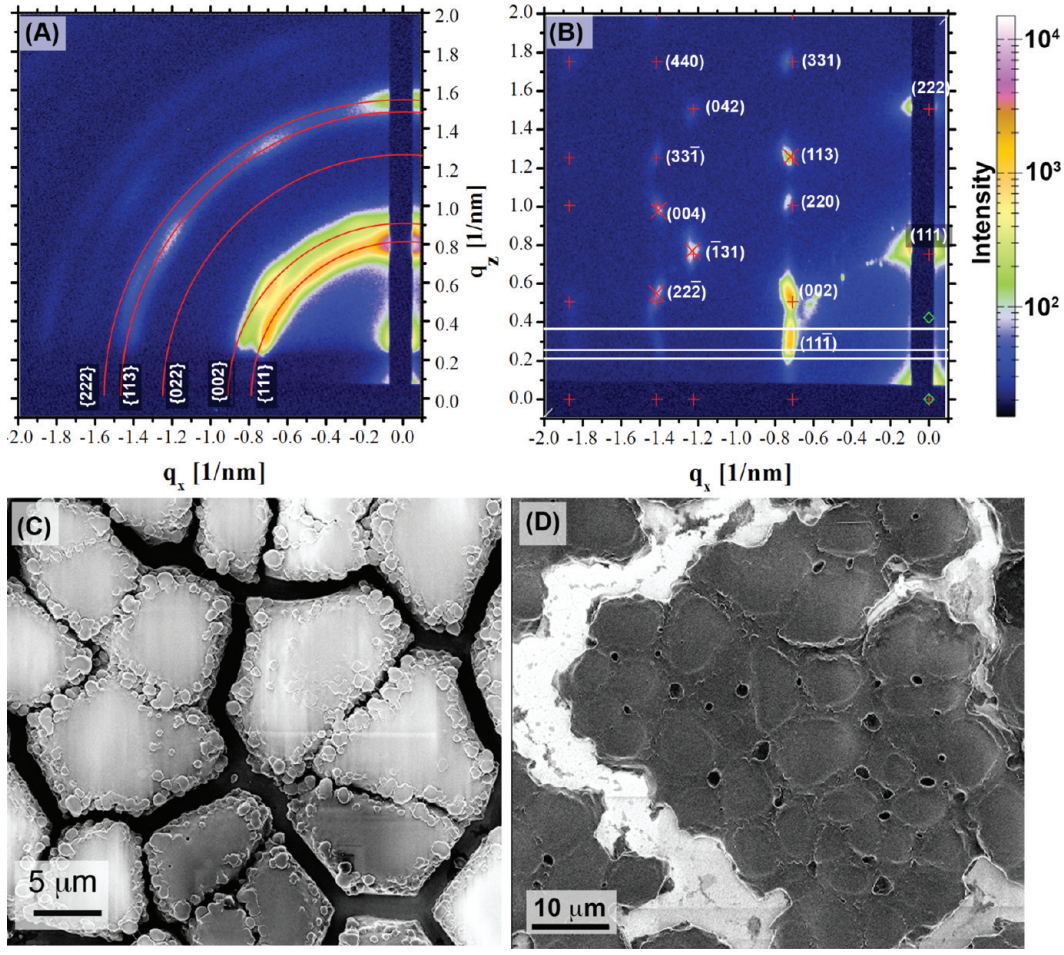

Figure 5. Solvent vapor annealing. GISAXS pattern of PbSe NC film drop cast onto Si before (A) and after (B) octane vapor annealing. SEM images of the corresponding films before (C) and after (D) solvent annealing.

tice shrinkage. Considering the similarity in NC size, surface chemistry, and chemical composition of PbS and PbSe NC cores, we conjecture that the superior spatial coherence in PbS NC films is due to the slightly narrower relative size distribution 9% in PbS NCs *versus* 11% in PbSe NCs used in this study (see Supporting Information Figure S16).

Analysis of Bragg peak broadening provides important insights into the extent of spatial coherence of the NC supracrystal. Using the Scherrer equation, we can quantify the supracrystal grain size from the peak width of the azimuthally integrated intensity profiles. In fast-dried PbSe and PbS NC films, the supracrystal grain sizes calculated from the $(111)_s$ reflection are approximately twice as large as those calculated from the $(002)_s$ reflection (~70 nm) (see Supporting Information Figure S12). Slowly dried NC films show a different trend. The width of $(111)_s$ and $(002)_s$ reflections are approximately equal in PbSe NC films, whereas in slowly dried PbS supracrystals the $(111)_s$ Bragg peak is 50% broader than the corresponding $(002)_s$ peak. The corresponding supracrystal grain sizes are calculated as 94 and 150 nm, respectively. This analysis quantitatively confirms that the extent of NC ordering correlates positively with the solvent evaporation time. Compared to the quickly dried films, the doubling of the grain size calculated from the $(002)_s$ reflections can be interpreted as a substantial improvement of NC ordering in the plane of the film. The anisotropic $(111)_s$ and $(002)_s$ peak width warrant further discussion. In molecular crystals, such anisotropies in Bragg peak widths are attributed to stress and strain effects in the crystal. A similar conclusion can be reached about distortions of the NC supracrystal during rapid solvent evaporation. We have recently applied *in situ* GISAXS to probe these aspects in more detail and will report the results in an upcoming report.[64]

Solvent Vapor Annealing. To date, efforts to improve the NC superlattice ordering have mostly focused on modifications to the NC/solvent or NC/substrate interactions.[61,65,70−72] Here, we present a complementary method directed at reordering of NC films already deposited on a substrate. Solvent vapor annealing (SVA) has been shown to improve spatial coherence in polymer films,[45,73,74] so we anticipated that a similar approach, applied to NC films, may enhance the ordering and mitigate the detrimental formation of microscopic cracks. The literature provides limited reports of vapor

sorption and capillary condensation in NC films[4,75] and, to the best of our knowledge, this work presents the first demonstration of solvent vapor annealing in NC films.

Figure 5 shows GISAXS patterns and low-resolution SEM images summarizing the effects of SVA. The initial PbS NC film was formed by drop-casting a 50 mg/mL suspension at a fast drying time of 3 min. The as-deposited sample is characterized by a ringlike GISAXS pattern (Figure 5A) and cracked supracrystal grains with sizes on the order of 5−10 μm (Figure 5C). We exposed the NC film to a saturated octane vapor environment for 8 h and then allowed the wet film to dry over the course of 4 min. Following the vapor annealing treatment, both GISAXS and SEM reveal significant structural changes to the NC assembly. The GISAXS pattern of the solvent annealed PbS NC film (Figure 5B) shows distinct scattering peaks that could be indexed to a $(111)_s$ oriented superlattice (a = 14.5 nm; 1% vertical shrinkage). The comparison of azimuthally and radially integrated intensity profiles of NC films before and after vapor exposure provide a clear illustration of the positive effects of SVA on the spatial coherence of NC films. The radial peak width of the $(111)_s$ reflection remained essentially unchanged, whereas the width of the $(002)_s$ reflection was nearly reduced by half, indicating a profound improvement in the NC supracrystal ordering parallel to the substrate (see Supporting Information Figure S13).

In addition to the improved long-range order obtained from the radial profiles, we analyzed the scattering intensity as a function of azimuthal angle (ϕ). The azimuthal intensity profiles show a dramatic sharpening of the $(002)_s$ reflection near 55°. The width of the initially disordered NC film (full width at half-maximum, $\delta\phi_{(002)}$ = 14°) was reduced by over 70% compared to the narrow $(002)_s$ reflection of the solvent annealed film ($\delta\phi_{(002)}$ = 4.1°) (see Supporting Information Figure S13B) Presumably, exposure to octane vapor led to capillary condensation[4,75] and transformed the film into a "liquidlike" suspension in which the NC have sufficient mobility to recrystallize, upon drying, in a highly ordered, lower energy configuration. The observation of higher order scattering features and the sharpening of peaks in the integrated intensity profiles are a clear testament to the success of SVA in enhancing the long-range spatial and orientational NC supracrystal ordering relative to the substrate.

The SEM image of the solvent-annealed NC film suggests that grains of the initial film merged to form larger grains with sizes on the order of ~50 μm. Unfortunately, the solvent annealed film still show macroscopic film cracks, which presumably formed during the isotropic volume contraction accompanying the gradual reduction in solvent vapor concentration. Further detailed *in situ* investigation of evaporation dynamics is required to minimize or avoid the formation of cracks in drying NC films.

A unique advantage of solvent annealing over thermal treatments is the ability to tune the solvent/NC interactions through choice of solvent. The results in Figure 5 illustrate the action of alkane solvents (*e.g.,* octane) as swelling agents, which introduces the ability to continuously adjust the NC superlattice spacing and opens the door to many exciting possibilities to tune the interactions between the NCs within the assembly.

Ligand Replacement. Beyond inert solvents just swelling the NC films, another promising dimension of vapor processing is the use of vapors that chemically interact with the ligands on the NC surface. For example, alcohols, thiols, and amines are known to exchange or displace oleate from the surface of lead salt NCs.[13,19,76,59] We discuss solvent vapor annealing with 1,2-ethanedithiol (EDT) as an illustrative example of this approach. We subjected highly ordered PbSe and PbS NC films to a saturated EDT vapor environment for 1 h followed by a rinse in acetonitrile to remove unbound oleic acid. On the basis of previous reports of solution phase dithiol treatments,[31] we expected EDT vapor treatment to partially remove oleic acid ligands from the NC surface and thereby reduce the average interparticle separation. FTIR spectroscopy allowed us to monitor the relative concentration of oleate ligands bound to the NC surface. Figure 6D shows FTIR spectra of lead salt NC films subjected to EDT vapor compared to control samples merely rinsed with acetonitrile. In both cases of PbSe and PbS NCs, EDT vapor treatment resulted in a noticeable reduction in CH stretching absorption features near 2900 cm^{-1}.

Using the previously discussed PbS and PbSe NC films as reference points (Figure 5B and 5D), GISAXS shows that EDT vapor treatment nearly completely disordered the NC assemblies. The scattering patterns in Figure 6 show that the loss of spatial coherence upon EDT vapor exposure was more pronounced in PbSe than in PbS. PbSe NC films treated with EDT vapor show a glassy GISAXS pattern without distinct scattering features (Figure 6A).

This observation is consistent with a previous report by Nozik and co-workers, who showed a loss in PbSe NC superlattice order upon solution phase EDT treatment.[29] We have previously shown that the displacement of surface bound ligands may degrade the single nanocrystal character through dipole-mediated oriented attachment or sintering.[19] However, in the case of EDT vapor treatment, SEM images of monolayer PbSe NC films confirmed that the structural integrity of individual NCs was preserved during EDT vapor exposure (see Supporting Information Figure S14).

PbS NC films treated with EDT vapor show diffuse scattering peaks superimposed on an amorphous background (Figure 6C). The scattering peaks could be in-

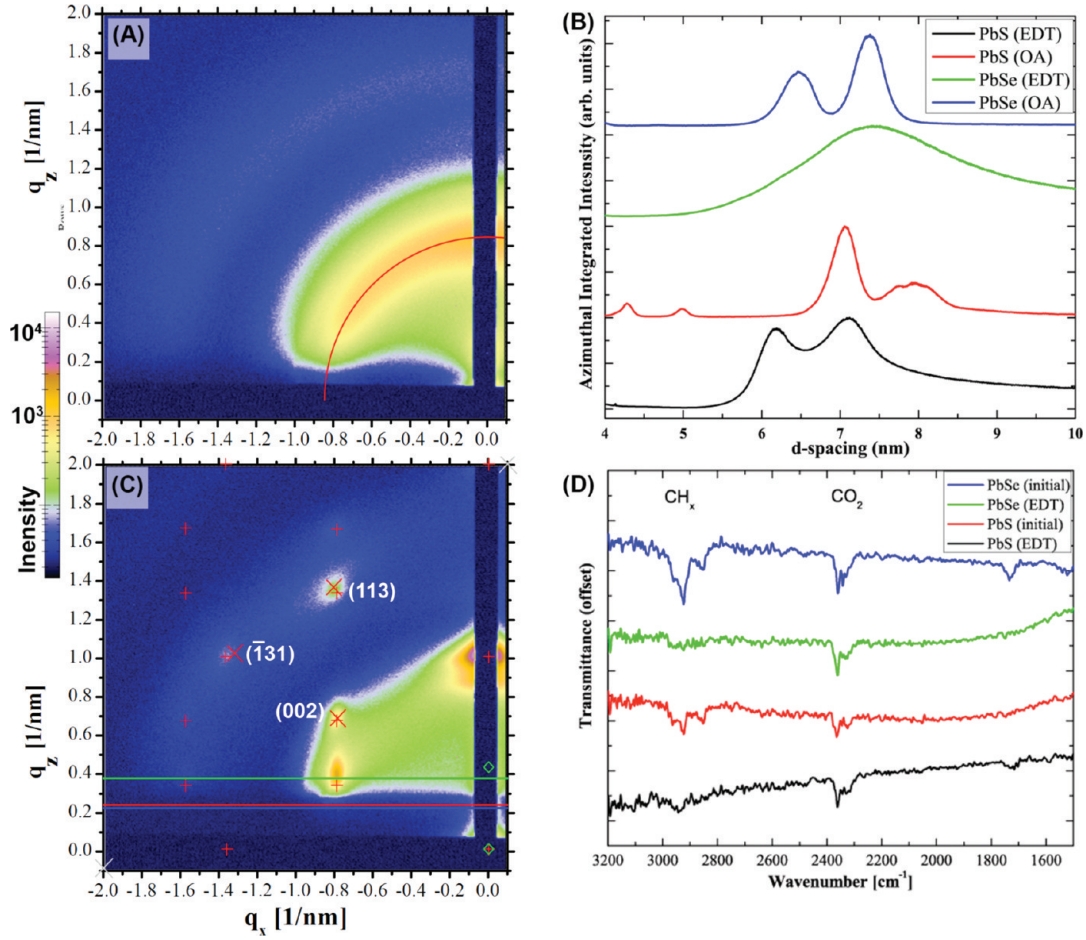

Figure 6. EDT vapor annealing. GISAXS pattern of drop-cast NC films after 1 h of EDT vapor exposure. Disordered PbSe NC (A) and partially ordered PbS NC film (C). (B) Azimuthally integrated GISAXS intensity profiles of the corresponding NC films before and after EDT vapor exposure. (D) FTIR spectra of NC films exposed to EDT vapor and unexposed control films.

dexed as the $(002)_s$, $(-131)_s$, and $(113)_s$ peaks of a distorted FCC(111) superlattice with $a = 13.0$ nm and a 20% shrinkage normal to the substrate plane. Considering the average NC diameter, $d_{nc} = 6.4$ nm, determined from TEM image analysis, and the nearest-neighbor direction $D_{NN} = \sqrt{2}a/2 = 9.2$ nm, we calculated the average interparticle separation of the EDT-vapor treated film to be 2.8 nm. This corresponds to a 0.9 nm reduction in interparticle separation compared to $D_{NN} = 10.1$ nm of the initial NC assembly (Figure 4D). This reduction of interparticle separation is approximately half the reduction reported for solution-phase EDT treatments in PbSe NC films.[29] The variance between our results and those reported by Nozik and coworkers[29] could be due to either (i) limitations of vapor-based EDT ligand displacement treatments or (ii) inherent differences in surface chemistry of PbS and PbSe. To distinguish between these two interpretations we exposed PbS NC films to a solution of EDT in ethanol. We found that even a brief (30 s) submersion of the PbS NC film in a 0.005 M EDT solution EDT in ethanol (EtOH) reduced the interparticle separation by 1.7−0.6 nm—consistent with the reports in the literature.[29] In a control experiment we submerged a PbS NC film in pure EtOH. This treatment reduced the interparticle separation to a similar extent as the EDT vapor treatment discussed above (see Supporting Information Figure S15). We note that, in stark contrast to the EDT vapor and solution treatments, EtOH treatment did not degrade the ordering of the PbS NC films as evidenced by the polycrystalline GISAXS scattering signature (see Supporting Information Figure S15).

Lastly, as a parallel to the comparison of highly ordered PbSe and PbS NC films shown in Figure 4, we point out that PbS NC films were able to partially preserve spatial coherence during EDT vapor treatment, whereas PbSe NC films were completely disordered upon exposure to EDT vapor. This comparison provides another line of evidence pointing toward stronger cohesive forces for supracrystal formation and coherence in PbS compared to PbSe NC films. Studies to understand the molecular origin of this difference are currently under way and we tentatively point to dissimilarities in faceting and surface chemistry in the lead salt NC family as the most likely factors.

CONCLUSION

We combined electron microscopy and grazing incidence X-ray scattering to investigate structural aspects of strongly coupled lead salt NC assemblies. The structure of PbSe NC films spun-cast onto Si and ITO exhibited similar features despite differences in substrate roughness. We observed submicrometer rectangular supracrystals with $(001)_s$ planes parallel to the substrate on top of a thin NC film with hexagonal symmetry. Drop-cast NC films show a pronounced correlation between NC ordering and orientation and processing conditions including the nature of the substrate and solvent evaporation kinetics. NC films drop-cast on silicon wafers formed remarkably well-ordered FCC superlattices with $(111)_s$ planes parallel to the substrate. In contrast, deposition on rougher ITO and PEDOT-coated ITO substrates resulted in polycrystalline NC assemblies with interparticle spacing similar to those measured in ordered NC films formed on Si. We probed the evaporation dynamics of the drop-casting process further by depositing NCs in a saturated vapor environment. Temporally extending the solvent evaporation by drop casting NC films in a saturated vapor environment showed profoundly enhanced spatial coherence compared to quickly dried NC films prepared in a dry atmosphere.

We demonstrated solvent vapor annealing as a promising post deposition technique to improve long-range ordering and supracrystal orientation in NC films. Initially polycrystalline NC films were transformed to highly oriented NC supracrystals upon exposure to octane vapor. Similar solvent vapor treatment with EDT resulted in ligand displacement accompanied by a pronounced reduction in NC ordering. EDT treated PbSe films were completely disordered, whereas PbS NC films preserved partial ordering. Taken together, these results provide important new insights into the NC structure/processing relationship of strongly coupled NC assemblies.

METHODS

Nanocrystal Synthesis. PbSe NCs were prepared following the method reported by Yu *et al.*[77] The synthesis was carried out in a three-necked flask under an inert nitrogen atmosphere. In a typical synthesis, PbO (4 mmol) and oleic acid (10 mmol) were dissolved in 1-octadecene (ODE) to yield a precursor solution with [Pb] = 0.3 M and a molar Pb/oleic acid ratio of 1:2.5. The solution was then degassed by heating to 160 °C for 1 h under flowing nitrogen. In a glovebox, Se was dissolved in trioctylphosphine (TOP) to yield a 1 M stock solution. A small amount of diphenylphospine (DPP) (4.5 mM) was added to the TOPSe solution. a 12 mL portion of the 1 M TOP−Se solution was rapidly injected into the vigorously stirred, hot lead oleate solution. PbSe NCs formed immediately after injection and their size was tuned through adjustments in temperature (120−180 °C), reaction time (0.5−5 min), and molar Pb/oleic acid ratio (1:6 to 1:3). After the elapsed reaction time, the solution was quenched by transferring the flask to a water bath. Following synthesis, the NCs were washed several times by sequential precipitation with ethanol and redispersion in anhydrous hexane. On the basis of statistical analysis of TEM images, it was determined that the PbSe NC cores had an average diameter of 6.1 nm with a 11% relative size distribution (see Supporting Information Figure S16).

The PbS synthesis was adopted from the work by Hines and Scholes.[78] For the synthesis of 8 nm PbS NCs, PbO (1 mmol) and oleic acid (25 mmol) were dissolved in approximately 2 mL ODE to yield a solution with a total volume of 10 mL. The solution was then degassed by heating to 150 °C for 1 h under flowing nitrogen. In a glovebox, 0.6 mol of bis(trimethylsilyl)sulfide (TMS) was dissolved in 6 mL of ODE and stirred thoroughly; 5 mL of the TMS solution was rapidly injected into the vigorously stirred, hot lead oleate solution. PbS NCs formed immediately after injection, and they were collected after 1 min of reaction at 150 °C. Following synthesis the NCs were washed several times by sequential precipitation with ethanol and redisperson in anhydrous hexane. On the basis of statistical analysis of TEM images, it was determined that the PbS NCs had an average diameter of 6.4 nm with a 9% relative size distribution (see Supporting Information Figure S16).

Substrate Preparation. Silicon wafers were cleaned by sequential sonication in deionized water and acetone followed by ozone plasma treatment. ITO substrates were cleaned by chemical mechanical polishing in soap solution, followed by sonication in deionized water and isopropyl alcohol and ozone plasma treatment.

Deposition Techniques. Our NC films were deposited either by spin-casting (1000 rpm; 60 s) or drop-casting from a colloidal suspension onto cleaned substrates. Spin-casting is recognized as a robust and well-controlled technique for the processing of homogeneous thin films. On the other hand the drop-casting process is complicated by a number of nonequilibrium processes. Our experimental setup was designed to minimize the impact of dynamic artifacts as far as possible (see Supporting Information Figure S17). Drop-cast films were allowed to evaporate either in a dry environment or in a controlled saturated vapor environment. We tuned the solvent evaporation rate by adjusting the amount of solvent in the reservoir and vapor exposure period. After the specific vapor exposure time, the top of an inverted funnel was unplugged to ensure slow diffusion-controlled evaporation of solvent from the control volume (see Supporting Information Figure S17). In a typical thin film preparation 50 μL of a colloidal NC suspension (0.05−50 mg/mL in hexane/octane 9:1 v/v) were dropcast onto 10−10 mm substrates.

Poly(3,4-ethylenedioxythiophene) poly(styrenesulfonate) (PEDOT:PSS) films were prepared by spin-casting the polymer suspension onto plasma cleaned indium tin oxide (ITO substrates). Then lead salt NCs were successively drop-cast onto the PEDOT:PSS film, as described above.

Electron and Atomic Force Microscopy. Transmission electron microscope (TEM) samples were prepared by drop casting diluted NC solutions onto carbon-coated 300 mesh Cu TEM grids. TEM images were taken on either an FEI Tecnai 20 (type Sphera) operated with a 200 kV LaB_6 filament or an FEI Titan equipped with a 300 kV field emission gun. Scanning electron microscope (SEM) imaging was acquired with a LEO 1550 FESEM operated at accelerating voltages ranging from 1.0 to 20 kV. Atomic force microscopy (AFM) characterization of substrate roughness was carried out on a Veeco Dimension 3100 Ambient AFM.

GISAXS. Grazing incidence small-angle X-ray scattering (GISAXS) measurements were performed on beamline D1 of the Cornell High Energy Synchrotron Source (CHESS) using monochromatic radiation of wavelength $\lambda = 1.284$ Å with a bandwidth $\Delta\lambda/\lambda$ of 1.5%.[34] The X-ray beam was produced by a hardbent dipole magnet of the Cornell storage ring and monochromatized with Mo:B_4C synthetic multilayers with a period of 30 Å. The D1 area detector (MedOptics) is a fiber-coupled CCD camera with a pixel size of 46.9 μm by 46.9 μm and a total of 1024 × 1024 pixels with a 14-bit dynamical range per pixel. Typical read-out time per image was below 5 s. The images were dark current corrected, distortion-corrected, and flat-field corrected by the acqui-

sition software.[79] The sample to detector distance was 938 mm, as determined using a silver behenate powder standard. The incident angle of the X-ray beam was varied between 0.02° to 0.45°; most data presented here were taken at 0.25°, that is, slightly above the silicon critical angle. Typical exposure times ranged from 0.1 to 1.0 s. Scattering images were calibrated and integrated using the Fit2D software.[80] GISAXS peaks were indexed and fitted using our in-house software.[81]

Acknowledgment. We thank Matthew Oh for assistance with the synthesis of the nanocrystals and Will Baumgardner for assistance with the FTIR measurements. This work was further funded in part by the KAUST-CU Center for Energy and Sustainability. J.J.C. was supported by the NSF IGERT Fellowship Program "Nanoscale Control of Surfaces and Interfaces." GISAXS measurements were conducted at the Cornell High Energy Synchrotron Source (CHESS) which is supported by the National Science Foundation and the National Institutes of Health/National Institute of General Medical Sciences under NSF award DMR-0225180. TEM images were acquired at the Soft Matter CryoTEM Research Unit at the Technical University of Eindhoven in work sponsored by the Joint Solar Programme (JSP) of the Stichting voor Fundamenteel Onderzoek der Materie FOM, which is supported financially by Nederlandse Organisatie voor Wetenschappelijk Onderzoek (NWO). The JSP is cofinanced by Gebied Chemische Wetenschappen of the NWO and Stichting Shell Research. SEM images were taken at the Cornell Center for Materials Research.

Supporting Information Available: Histogram of PbSe and PbS NC core diameters; experimental setup used to drop-cast NC films in a controlled vapor environment; SEM images of ravioli-shaped PbSe NC supracrystals; AFM images of ITO and PEDOT-coated ITO substrates; angle-resolved GISAXS patterns of spin-cast and drop-cast NC films; SEM images of cracked NC films; GISAXS patterns of NC films deposited onto PEDOT-coated ITO substrates and GISAXS patterns of NC films before and after exposure to vapor and solution phase EDT treatment. This material is available free of charge *via* the Internet at http://pubs.acs.org.

REFERENCES AND NOTES

1. Adams, D. M.; Brus, L.; Chidsey, C. E. D.; Creager, S.; Creutz, C.; Kagan, C. R.; Kamat, P. V.; Lieberman, M.; Lindsay, S.; Marcus, R. A.; *et al.* Charge Transfer on the Nanoscale: Current Status. *J. Phys. Chem. B* **2003**, *107*, 6668–6697.
2. Feldheim, D. L.; Keating, C. D. Self-Assembly of Single Electron Transistors and Related Devices. *Chem. Soc. Rev.* **1998**, *27*, 1–12.
3. Kamat, P. V. Photophysical, Photochemica, And Photocatalytic Aspects of Metal Nanoparticles. *J. Phys. Chem. B* **2002**, *106*, 7729–7744.
4. Krasteva, N.; Fogel, Y.; Bauer, R. E.; Mullen, K.; Joseph, Y.; Matsuzawa, N.; Yasuda, A.; Vossmeyer, T. Vapor Sorption and Electrical Response of Au-Nanoparticle−Dendrimer Composites. *Adv. Funct. Mater.* **2007**, *17*, 881–888.
5. Markovich, G.; Collier, C.; Henrichs, S.; Remacle, F.; Levine, R.; Heath, J. Architectonic Quantum Dot Solids. *Acc. Chem. Res.* **1999**, *32*, 415–423.
6. Wise, F. W. Lead Salt Quantum Dots: The Limit of Strong Quantum Confinement. *Acc. Chem. Res.* **2000**, *33*, 773–780.
7. Efros, A. L.; Efros, A. L. *Sov. Phys. Semicond.* **1982**, *16*, 772–779.
8. Jiang, X. M.; Schaller, R. D.; Lee, S. B.; Pietryga, J. M.; Klimov, V. I.; Zakhidov, A. A. PbSe Nanocrystal/Conducting Polymer Solar Cells with an Infrared Response to 2 Micron. *J. Mater. Res.* **2007**, *22*, 2204–2210.
9. Du, H.; Chen, C. L.; Krishnan, R.; Krauss, T. D.; Harbold, J. M.; Wise, F. W.; Thomas, M. G.; Silcox, J. Optical Properties of Colloidal PbSe Nanocrystals. *Nano Lett.* **2002**, *2*, 1321–1324.
10. Pietryga, J. M.; Schaller, R. D.; Werder, D.; Stewart, M. H.; Klimov, V. I.; Hollingsworth, J. A. Pushing the Band Gap Envelope: Mid-Infrared Emitting Colloidal PbSe Quantum Dots. *J. Am. Chem. Soc.* **2004**, *126*, 11752–11753.
11. Cui, D.; Xu, J.; Zhu, T.; Paradee, G.; Ashok, S. Harvest of near Infrared Light in PbSe Nanocrystal-Polymer Hybrid Photovoltaic Cells. *Appl. Phys. Lett.* **2006**, *88*, 183111.
12. Evans, C.; Guo, L.; Peterson, J.; Maccagnano-Zacher, S.; Krauss, T. Ultrabright PbSe Magic-Sized Clusters. *Nano Lett.* **2008**, *8*, 2896–2899.
13. Talapin, D. V.; Murray, C. B. PbSe Nanocrystal Solids for *n*- and *p*-Channel Thin Film Field-Effect Transistors. *Science* **2005**, *310*, 86–89.
14. Luther, J. M.; Beard, M. C.; Song, Q.; Law, M.; Ellingson, R. J.; Nozik, A. J. Multiple Exciton Generation in Films of Electronically Coupled PbSe Quantum Dots. *Nano Lett.* **2007**, *7*, 1779–1784.
15. Beard, M. C.; Midgett, A. G.; Law, M.; Semonin, O. E.; Ellingson, R. J.; Nozik, A. J. Variations in the Quantum Efficiency of Multiple Exciton Generation for a Series of Chemically Treated PbSe Nanocrystal Films. *Nano Lett.* **2009**, *9*, 836–845.
16. Cho, K.-S.; Talapin, D. V.; Gaschler, W.; Murray, C. B. Designing PbSe Nanowires and Nanorings through Oriented Attachment of Nanoparticles. *J. Am. Chem. Soc.* **2005**, *127*, 7140–7147.
17. Shim, M.; Guyot-Sionnest, P. Permanent Dipole Moment and Charges in Colloidal Semiconductor Quantum Dots. *J. Chem. Phys.* **1999**, *111*, 6955–6964.
18. Cho, K.-S.; Talapin, D. V.; Gaschler, W.; Murray, C. B. Designing PbSe Nanowires and Nanorings through Oriented Attachment of Nanoparticles. *J. Am. Chem. Soc.* **2005**, *127*, 7140–7147.
19. Hanrath, T.; Veldman, D.; Choi, J. J.; Christova, C. G.; Wienk, M. M.; Janssen, R. A. J. PbSe Nanocrystal Network Formation during Pyridine Ligand Displacement. *ACS Appl. Mater. Interfaces* **2009**, *1*, 244–250.
20. Talapin, D. V.; Shevchenko, E. V.; Murray, C. B.; Titov, A. V.; Kral, P. Dipole-Dipole Interactions in Nanoparticle Superlattices. *Nano Lett.* **2007**, *7*, 1213–1219.
21. Klokkenburg, M.; Houtepen, A. J.; Koole, R.; De Folter, J. W. J.; Erne, B. H.; Van Faassen, E.; Vanmaekelbergh, D. Dipolar Structures in Colloidal Dispersions of PbSe and CdSe Quantum Dots. *Nano Lett.* **2007**, *7*, 2931–2936.
22. Murray, C. B.; Sun, S. H.; Gaschler, W.; Doyle, H.; Betley, T. A.; Kagan, C. R. Colloidal Synthesis of Nanocrystals and Nanocrystal Superlattices. *IBM J. Res. Dev.* **2001**, *45*, 47–56.
23. Xia, Y. N.; Gates, B.; Yin, Y. D.; Lu, Y. Monodispersed Colloidal Spheres: Old Materials with New Applications. *Adv. Mater.* **2000**, *12*, 693–713.
24. Harfenist, S. A.; Wang, Z. L.; Alvarez, M. M.; Vezmar, I.; Whetten, R. L. Highly Oriented Molecular Ag Nanocrystal Arrays. *J. Phys. Chem.* **1996**, *100*, 13904–13910.
25. Korgel, B. A.; Fullam, S.; Connolly, S.; Fitzmaurice, D. Assembly and Self-Organization of Silver Nanocrystal Superlattices: Ordered Soft Spheres. *J. Phys. Chem. B* **1998**, *102*, 8379–8388.
26. Ball, P. *The Self-Made Tapestry: Pattern Formation in Nature;* Oxford University Press: New York, 1998.
27. Koleilat, G. I.; Levina, L.; Shukla, H.; Myrskog, S. H.; Hinds, S.; Pattantyus-Abraham, A. G.; Sargent, E. H. Efficient, Stable Infrared Photovoltaics Based on Solution-Cast Colloidal Quantum Dots. *ACS Nano* **2008**, *2*, 833–840.
28. Sargent, E. H. Solution-Processed Infrared Optoelectronics: Photovoltaics, Sensors, And Sources. *IEEE J. Sel. Top. Quantum Electron.* **2008**, *14*, 1223–1229.
29. Luther, J. M.; Law, M.; Song, Q.; Perkins, C. L.; Beard, M. C.; Nozik, A. J. Structural, Optical, and Electrical Properties of Self-Assembled Films of PbSe Nanocrystals Treated with 1,2-Ethanedithiol. *ACS Nano* **2008**, *2*, 271–280.
30. Luther, J. M.; Law, M.; Beard, M. C.; Song, Q.; Reese, M. O.; Ellingson, R. J.; Nozik, A. J. Schottky Solar Cells Based on Colloidal Nanocrystal Films. *Nano Lett.* **2008**, *8*, 3488–3492.
31. Law, M.; Luther, J. M.; Song, O.; Hughes, B. K.; Perkins, C. L.; Nozik, A. J. Structural, Optical, And Electrical Properties of PbSe Nanocrystal Solids Treated Thermally or with Simple Amines. *J. Am. Chem. Soc.* **2008**, *130*, 5974–5985.

32. Sigman, M. B.; Saunders, A. E.; Korgel, B. A. Metal Nanocrystal Superlattice Nucleation and Growth. *Langmuir* **2004**, *20*, 978–983.
33. The subscript s denotes either the direction of the [*hkl*]s superlattice normal or (*hkl*)s planes parallel to the substrate.
34. Smilgies, D.-M.; Busch, P.; Posselt, D.; Papadakis, C. M. Characterization of Polymer Thin Films with Small-Angle X-ray Scattering under Grazing Incidence (GISAXS). *Synchrotron Radiat. News* **2002**, *15*, 35–41.
35. Gibaud, A.; Grosso, D.; Smarsly, B.; Baptiste, A.; Bardeau, J. F.; Babonneau, F.; Doshi, D. A.; Chen, Z.; Brinker, C. J.; Sanchez, C. Evaporation-Controlled Self-Assembly of Silica Surfactant Mesophases. *J. Phys. Chem. B* **2003**, *107*, 6114–6118.
36. Du, P.; Li, M.; Douki, K.; Li, X.; Garcia, C. B. W.; Jain, A.; Smilgies, D.-M.; Fetters, L. J.; Gruner, S. M.; Wiesner, U.; *et al*. Additive-Driven Phase-Selective Chemistry in Block Copolymer Thin Films: The Convergence of Top-Down and Bottom-Up Approaches. *Adv. Mater.* **2004**, *16*, 953–957.
37. Li, M. Q.; Douki, K.; Goto, K.; Li, X. F.; Coenjarts, C.; Smilgies, D. M.; Ober, C. K. Spatially Controlled Fabrication of Nanoporous Block Copolymers. *Chem. Mater.* **2004**, *16*, 3800–3808.
38. Lee, B.; Park, I.; Yoon, J.; Park, S.; Kim, J.; Kim, K.-W.; Chang, T.; Ree, M. Structural Analysis of Block Copolymer Thin Films with Grazing Incidence Small-Angle X-ray Scattering. *Macromolecules* **2005**, *38*, 4311–4323.
39. Smarsly, B.; Gibaud, A.; Ruland, W.; Sturmayr, D.; Brinker, C. J. Quantitative SAXS Analysis of Oriented 2D Hexagonal Cylindrical Silica Mesostructures in Thin Films Obtained from Nonionic Surfactants. *Langmuir* **2005**, *21*, 3858–3866.
40. Narayanan, S.; Wang, J.; Lin, X.-M. Dynamical Self-Assembly of Nanocrystal Superlattices during Colloidal Droplet Evaporation by *in Situ* Small Angle X-ray Scattering. *Phys. Rev. Lett.* **2004**, *93*, 135503.
41. Saunders, A. E.; Ghezelbash, A.; Smilgies, D. M.; Sigman, M. B.; Korgel, B. A. Columnar self-assembly of colloidal nanodisks. *Nano Lett.* **2006**, *6*, 2959–2963.
42. Constantinides, M. G.; Jaeger, H. M.; Xuefa, L.; Jin, W.; Lin, X.-M. The Formation and Characterization of Three-Dimensional Gold Nanocrystal Superlattices. *Z. Kristallogr.* **2007**, *222*, 595–600.
43. Aleksandrovic, V.; Greshnykh, D.; Randjelovic, I.; Froemsdorf, A.; Kornowski, A.; Roth, S. V.; Klinke, C.; Weller, H. Preparation and Electrical Properties of Cobalt-Platinum Nanoparticle Monolayers Deposited by the Langmuir−Blodgett Technique. *ACS Nano* **2008**, *2*, 1123–1130.
44. Tate, M. P.; Eggiman, B. W.; Kowalski, J. D.; Hillhouse, H. W. Order and Orientation Control of Mesoporous Silica Films on Conducting Gold Substrates Formed by Dip-Coating and Self-Assembly: A Grazing Angle of Incidence Small-Angle X-ray Scattering and Field Emission Scanning Electron Microscopy Study. *Langmuir* **2005**, *21*, 10112–10118.
45. Bosworth, J. K.; Paik, M. Y.; Ruiz, R.; Schwartz, E. L.; Huang, J. Q.; Ko, A. W.; Smilgies, D. M.; Black, C. T.; Ober, C. K. Control of Self-Assembly of Lithographically Patternable Block Copolymer Films. *ACS Nano* **2008**, *2*, 1396–1402.
46. Crossland, E. J. W.; Kamperman, M.; Nedelcu, M.; Ducati, C.; Wiesner, U.; Smilgies, D.-M.; Toombes, G. E. S.; Hillmyer, M. A.; Ludwigs, S.; Steiner, U. A Bicontinuous Double Gyroid Hybrid Solar Cell. *Nano Lett.* **2008**, *9*, 2807–2812.
47. Dunphy, D.; Fan, H. Y.; Li, X. F.; Wang, J.; Brinker, C. J. Dynamic Investigation of Gold Nanocrystal Assembly Using *in Situ* Grazing-Incidence Small-angle X-ray Scattering. *Langmuir* **2008**, *24*, 10575–10578.
48. Smith, D.; Goodfellow, B.; Smilgies, D.; Korgel, B. Self-Assembled Simple Hexagonal AB 2Binary Nanocrystal Superlattices: SEM, GISAXS, and Defects. *J. Am. Chem. Soc.* **2009**, *131*, 3281–3290.
49. Renaud, G.; Lazzari, R.; Revenant, C.; Barbier, A.; Noblet, M.; Ulrich, O.; Leroy, F.; Jupille, J.; Borensztein, Y.; Henry, C. R. Real-Time Monitoring of Growing Nanoparticles. *Science* **2003**, *300*, 1378–1379.
50. Dourdain, S.; Rezaire, A.; Mehdi, A.; Ocko, B. M.; Gibaud, A. Real Time GISAXS Study of Micelle Hydration in CTAB Templated Silica Thin Films. *Phys. B* **2005**, *357*, 180–184.
51. Papadakis, C. M.; Di, Z. Y.; Posselt, D.; Smilgies, D. M. Structural Instabilities in Lamellar Diblock Copolymer Thin Films During Solvent Vapor Uptake. *Langmuir* **2008**, *24*, 13815–13818.
52. Metwalli, E.; Couet, S.; Schlage, K.; Rohlsberger, R.; Korstgens, V.; Ruderer, M.; Wang, W.; Kaune, G.; Roth, S. V.; Muüller-Buschbaum, P. *In Situ* GISAXS Investigation of Gold Sputtering onto a Polymer Template. *Langmuir* **2008**, *24*, 4265–4272.
53. Kaune, G.; Ruderer, M.; Metwalli, E.; Wang, W.; Couet, S.; Schlage, K.; Rouhlsberger, R.; Roth, S.; Muller-Buschbaum, P. *In Situ* GISAXS Study of Gold Film Growth on Conducting Polymer Films. *ACS Appl. Mater. Interfaces* **2009**, *1*, 353–360.
54. Smilgies, D.-M.; Li, R.; Di, Z.; Darko, C.; Papadaki, C. M.; Posselt, D. Probing the Self-Organization Kinetics in Block Copolymer Thin Films. *Mater. Res. Soc. Symp. Proc.* **2009**, 1147OO01−01.
55. Collier, C. P.; Vossmeyer, T.; Heath, J. R. Nanocrystal Superlattices. *Annu. Rev. Phys. Chem.* **1998**, *49*, 371–404.
56. Wang, Z. L. Structural Analysis of Self-Assembling Nanocrystal Superlattices. *Adv. Mater.* **1998**, *10*, 13.
57. Lin, X. M.; Jaeger, H. M.; Sorensen, C. M.; Klabunde, K. J. Formation of Long-Range Ordered Nanocrystal Superlattices on Silicon Nitride Substrates. *J. Phys. Chem. B* **2001**, *105*, 3353–3357.
58. Brinker, C. J.; Lu, Y. F.; Sellinger, A.; Fan, H. Y. Evaporation-Induced Self-Assembly: Nanostructures Made Easy. *Adv. Mater.* **1999**, *11*, 579.
59. Luther, J. M.; Law, M.; Song, Q.; Perkins, C. L.; Beard, M. C.; Nozik, A. J. Structural, Optical, and Electrical Properties of Self-Assembled Films of PbSe Nanocrystals Treated with 1,2-Ethanedithiol. *ACS Nano* **2008**, *2*, 271–280.
60. Luther, J. M.; Law, M.; Beard, M. C.; Song, Q.; Reese, M. O.; Ellingson, R. J.; Nozik, A. J. Schottky Solar Cells Based on Colloidal Nanocrystal Films. *Nano Lett.* **2008**, *8*, 3488–3492.
61. Murray, C. B.; Kagan, C. R.; Bawendi, M. G. Self-Organization of CdSe Nanocrystallites into 3-Dimensional Quantum Dot Superlattices. *Science* **1995**, *270*, 1335–1338.
62. Yoneda, Y. Anomalous Surface Reflection of X Rays. *Phys. Rev.* **1963**, *131*, 2010.
63. Busch, P.; Rauscher, M.; Smilgies, D. M.; Posselt, D.; Papadakis, C. M. Grazing-Incidence Small-Angle X-ray Scattering from Thin Polymer Films with Lamellar Structures—Tthe Scattering Cross Section in the Distorted-Wave Born Approximation. *J. Appl. Crystallogr.* **2006**, *39*, 433–442.
64. Bian, K.; Choi, J. J.; Hanrath, T.; Smilgies, D., in preparation.
65. Coe-Sullivan, S.; Steckel, J. S.; Woo, W. K.; Bawendi, M. G.; Bulovic, V. Large-Area Ordered Quantum-Dot Monolayers *via* Phase Separation during Spin-Casting. *Adv. Funct. Mater.* **2005**, *15*, 1117–1124.
66. Yan, Q.; Gao, L.; Sharma, V.; Chiang, Y. M.; Wong, C. C. Particle and Substrate Charge Effects on Colloidal Self-Assembly in a Sessile Drop. *Langmuir* **2008**, *24*, 11518–11522.
67. Ghosh, S.; Inganas, O. Electrochemical Characterization of Poly(3,4-ethylene dioxythiophene) Based Conducting Hydrogel Networks. *J. Electrochem. Soc.* **2000**, *147*, 1872–1877.
68. Tate, M. P.; Hillhouse, H. W. General Method for Simulation of 2D GISAXS Intensities for Any Nanostructured Film Using Discrete Fourier Transforms. *J. Phys. Chem. C* **2007**, *111*, 7645–7654.
69. Bigioni, T. P.; Lin, X. M.; Nguyen, T. T.; Corwin, E. I.; Witten, T. A.; Jaeger, H. M. Kinetically Driven Self Assembly of Highly Ordered Nanoparticle Monolayers. *Nat. Mater.* **2006**, *5*, 265–270.

70. Shevchenko, E. V.; Talapin, D. V.; Kotov, N. A.; O'Brien, S.; Murray, C. B. Structural Diversity in Binary Nanoparticle Superlattices. *Nature* **2006**, *439*, 55–59.
71. Tang, Z. Y.; Zhang, Z. L.; Wang, Y.; Glotzer, S. C.; Kotov, N. A. Self-Assembly of CdTe Nanocrystals into Free-Floating Sheets. *Science* **2006**, *314*, 274–278.
72. Redl, F. X.; Cho, K. S.; Murray, C. B.; O'Brien, S. Three-Dimensional Binary Superlattices of Magnetic Nanocrystals and Semiconductor Quantum Dots. *Nature* **2003**, *423*, 968–971.
73. Sidorenko, A.; Tokarev, I.; Minko, S.; Stamm, M. Ordered Reactive Nanomembranes/Nanotemplates from Thin Films of Block Copolymer Supramolecular Assembly. *J. Am. Chem. Soc.* **2003**, *125*, 12211–12216.
74. Kim, S. H.; Misner, M. J.; Yang, L.; Gang, O.; Ocko, B. M.; Russell, T. P. Salt Complexation in Block Copolymer Thin Films. *Macromolecules* **2006**, *39*, 8473–8479.
75. Gemici, Z.; Schwachulla, P. I.; Williamson, E. H.; Rubner, M. F.; Cohen, R. E. Targeted Functionalization of Nanoparticle Thin Films *via* Capillary Condensation. *Nano Lett.* **2009**, *9*, 1064–1070.
76. Law, M.; Luther, J. M.; Song, O.; Hughes, B. K.; Perkins, C. L.; Nozik, A. J. Structural, Optical, And Electrical Properties of PbSe Nanocrystal Solids Treated Thermally or with Simple Amines. *J. Am. Chem. Soc.* **2008**, *130*, 5974–5985.
77. Yu, W. W.; Falkner, J. C.; Shih, B. S.; Colvin, V. L. Preparation and Characterization of Monodisperse PbSe Semiconductor Nanocrystals in a Non-coordinating Solvent. *Chem. Mater.* **2004**, *16*, 3318–3322.
78. Hines, M. A.; Scholes, G. D. Colloidal PbS Nanocrystals with Size-Tunable Near-Infrared Emission: Observation of Post-Synthesis Self-Narrowing of the Particle Size Distribution. *Adv. Mater.* **2003**, *15*, 1844–1849.
79. Gruner, S. M.; Tate, M. W.; Eikenberry, E. F. Charge-Coupled Device Area X-ray Detectors. *Rev. Sci. Instrum.* **2002**, *73*, 2815–2842.
80. Hammersley, A. P. *ESRF97HA02T FIT2D: An Introduction and Overview*; ESRF Internal Report; ESRF: Grenoble, France, 1997.
81. Smilgies, D. M.; Blasini, D. R. Indexation Scheme for Oriented Molecular Thin Films Studied with Grazing-Incidence Reciprocal-Space Mapping. *J. Appl. Crystallogr.* **2007**, *40*, 716–718.